Medical Image Analysis 24 (2015) 28–40

Contents lists available at ScienceDirect

Medical Image Analysis

journal homepage: www.elsevier.com/locate/media

Automated extraction and labelling of the arterial tree from whole-body MRA data

Rahil Shahzad[a,1,*], Oleh Dzyubachyk[a,1], Marius Staring[a], Joel Kullberg[b], Lars Johansson[b], Håkan Ahlström[b], Boudewijn P.F. Lelieveldt[a,c], Rob J. van der Geest[a]

[a] Division of Image Processing, Department of Radiology, Leiden University Medical Center, Leiden PO Box 9600, 2300 RC, The Netherlands
[b] Department of Radiology, Uppsala University Hospital, SE-751 85 Uppsala, Sweden
[c] Intelligent Systems Department, Delft University of Technology, PO Box 5031, 2600 GA Delft, The Netherlands

ARTICLE INFO

Article history:
Received 27 September 2014
Revised 9 May 2015
Accepted 13 May 2015
Available online 21 May 2015

Keywords:
Whole-body MRA
Intensity inhomogeneity correction
Vessel tree extraction
Atlas-based image registration
Graph matching

ABSTRACT

In this work, we present a fully automated algorithm for extraction of the 3D arterial tree and labelling the tree segments from whole-body magnetic resonance angiography (WB-MRA) sequences. The algorithm developed consists of two core parts (*i*) 3D volume reconstruction from different stations with simultaneous correction of different types of intensity inhomogeneity, and (*ii*) Extraction of the arterial tree and subsequent labelling of the pruned extracted tree. Extraction of the arterial tree is performed using the probability map of the "contrast" class, which is obtained as one of the results of the inhomogeneity correction scheme. We demonstrate that such approach is more robust than using the difference between the pre- and post-contrast channels traditionally used for this purpose. Labelling the extracted tree is performed by using a combination of graph-based and atlas-based approaches. Validation of our method with respect to the extracted tree was performed on the arterial tree subdivided into 32 segments, 82.4% of which were completely detected, 11.7% partially detected, and 5.9% were missed on a cohort of 35 subjects. With respect to automated labelling accuracy of the 32 segments, various registration strategies were investigated on a training set consisting of 10 scans. Further analysis on the test set consisting of 25 data sets indicates that 69% of the vessel centerline tree in the head and neck region, 80% in the thorax and abdomen region, and 84% in the legs was accurately labelled to the correct vessel segment. These results indicate clinical potential of our approach in enabling fully automated and accurate analysis of the entire arterial tree. This is the first study that not only automatically extracts the WB-MRA arterial tree, but also labels the vessel tree segments.

1. Introduction

1.1. Background

Recent developments in magnetic resonance (MR) systems, have enabled imaging of the whole body within reasonable time and with good image quality (Lauenstein and Semelka, 2006; Ruehm et al., 2001). The absence of harmful ionizing radiation has made MR very popular for acquiring MR angiography (MRA) scans (Ladd and Ladd, 2007). The feasibility of using whole-body MRA (WB-MRA) in the clinic for diagnosing arterial diseases and for general screening has been investigated by a number of groups (Goehde et al., 2005; Hansen et al., 2007; Tizon et al., 2007).

However, all the studies performed on WB-MRA scans for diagnosing arterial trees have been conducted manually and on maximum intensity projection (MIP) images (Goehde et al., 2005; Hansen et al., 2007; Lundberg et al., 2013). No extensive methods have been developed to investigate the possibility of extracting the arterial tree in 3D. One of the reasons for this is the difficulty with stitching and inhomogeneity correction of the WB-MRA scans, which are generally obtained using multiple stations. Here, by "stations" we refer to the different positions of the scanner bed during acquisition (Börnert and Aldefeld, 2008; Dzyubachyk et al., 2013). When it comes to automated labelling of the vessel tree, the complexity of the vascular structures makes this task more difficult. Having available a method for automated vessel tree labelling would enable comprehensive reporting of the arterial disease findings in a fully automated fashion.

By performing analysis and quantification on MIP images, the entire potential of WB-MRA scans is not being utilized. A method for automatic extraction of 3D vascular tree would be very useful for arterial disease analysis and quantification. Such an automated method

* Corresponding author. Tel.: +31 715262133.
E-mail address: r.shahzad@lumc.nl, rahilshahzad@gmail.com (R. Shahzad).
[1] Both authors contributed equally to this work.

http://dx.doi.org/10.1016/j.media.2015.05.008
1361-8415/

would especially be useful in population-based screening studies, like the ones performed by Ladd et al. (2007) or Lundberg et al. (2013).

1.2. Previous work

A rather limited amount of publications on reconstruction of 3D WB-MR volumes, including correction of different types of intensity inhomogeneity, is available. This can be explained by the relative novelty of the field itself. Several published methods considered either intensity normalization of multiple acquired image stacks (Jäger and Hornegger, 2009), or stitching of entire 3D volumes with simultaneous correction of geometrical distortions (Wachinger et al., 2008). A large array of the bias correction methods for MR data that has been published during past years (Pham and Prince, 1999; Sled et al., 1998; Van Leemput et al., 1999; Wells et al., 1996) was so far primarily developed and applied to neurological (brain) images, and feasibility of application of these methods to WB-MR data remains an open question. Our earlier work on joint intensity inhomogeneity correction (Dzyubachyk et al., 2013) remains with respect to the methodology of WB-MR volume reconstruction and bias correction the closest publication to the work presented here.

Vascular segmentation has had a lot of research interest, and several methods to segment various vessel trees within the body have been proposed. The review papers by Suri et al. (2002a; 2002b) extensively cover MR vascular image processing techniques. A more recent review article of Lesage et al. (2009) presents general techniques on 3D vessel lumen segmentation on different imaging modalities. In a broad sense, vascular segmentation methods can be divided into two categories: model-based and feature-based.

The extracted vascular tree is typically represented as a centerline tree. Most of the vessel centerline extraction methods generally focus on a particular anatomical region, such as the heart [(Schaap et al., 2009), evaluate methods for coronary artery centerline extraction], the neck [(Hameeteman et al., 2011), evaluate methods that segment the carotid arteries], brain [(Flasque et al., 2001), present a method for cerebral vessel tree segmentation], and lungs [(Lo et al., 2012; Rudyanto et al., 2014), compares algorithms for segmenting blood vessels and extracting the airway tree]. A few methods make use of an atlas for segmenting vessel structures, employing in this way the prior anatomical knowledge to drive the vessel segmentation. (Passat et al., 2006) use an atlas-based approach to segment the cerebral vessels, their method uses a combination of anatomical information from cerebral vascular atlases and local image features to help the segmentation process. Isgum et al. (2009) present a multi-atlas-based approach for delineating anatomical structures and its application for aorta segmentation.

Automated vessel segment labelling is a much more challenging task, and a few methods have investigated this possibility. Uchiyama et al. (2006) developed an image-registration-based method to label the cerebral arteries. Bogunović et al. (2013) label the cerebral arteries by using prior anatomical knowledge on an extracted vessel graph. Matsuzaki et al. (2015) present a method to label the vessel tree in the abdomen using a combination of rule-based and machine learning approaches. Yang et al. (2011) label the coronary arteries using a statistical coronary tree model. Gülsün et al. (2014) use geodesic paths between tree shapes to label the coronary arteries. Airway tree labelling is very similar to vessel tree labelling, Mori et al. (2000) developed a knowledge-based method for labelling the airway tree. Tschirren et al. (2005) present a method to label the anatomical segments in the airway tree that is based on graph matching.

All the aforementioned labelling methods: (*i*) focus on a fixed anatomical region (cerebral arteries, coronary arteries, abdominal vessels, airway tree); (*ii*) use an imaging protocol that was optimized for such purposes; and (*iii*) typically rely on prior knowledge of underlying anatomy. These reasons, in combination with a rather limited resolution of whole-body scans, make their direct application to WB-MRA data virtually impossible. In this work, we develop a method that uses a combination of image-based and graph-based approaches. Similar to the approach proposed by Uchiyama et al. (2006), we use an image-registration-based method to find correspondence between an unseen data set and a labelled image. However, due to the large variability in the whole-body arterial tree, an image registration alone is not sufficient for the purpose of vessel labelling. To address this problem, we incorporate a graph-based approach, similar to the work of Tschirren et al. (2005). However, unlike that approach, we do not rigidly register the subject tree to a population-average labelled tree, but rather use a multi-atlas-based image registration method to obtain an initial set of vessel labels. This labelled graph tree is subsequently refined by using a rule-based approach.

To the best of our knowledge, there is only one other method that performs extraction of a vessel tree from WB-MRA data (Tizon et al., 2007). However, in that work the vessel tree extraction was performed on 2D MIP data and requires a significant amount of user interaction. In addition, the authors do not perform prior intensity inhomogeneity correction or accurate 3D volume stitching.

Table 1
Labels used to represent the various vessels. Left and right branches (if present) get unique labels.

Vessel name	Assigned label
Femoral+popliteal arteries	1, 2
Aorta	3
Posterior tibial arteries	4, 5
Anterior tibial arteries	6, 7
Subclavian+axillary arteries	8, 9
Vertebral arteries	10, 11
External iliac arteries	12, 13
Fibular arteries	14, 15
Deep femoral arteries	16, 17
Internal carotid arteries	18, 19
Common carotid arteries	20, 21
Internal iliac arteries	22, 23
Common iliac arteries	24, 25
Renal arteries	26, 27
External carotid arteries	28, 29
Brachiocephalic trunk	30
Superior mesenteric artery	31
Celiac trunk	32

1.3. Proposed method

In this paper, we present a novel method that enables accurate automated extraction and labelling of the arterial vascular tree from WB-MRA scans. To our knowledge, this is the first completely automatic method that extracts and labels the 3D vascular tree from the WB-MRA data. The main novelty of our approach is multi-fold: (*i*) We treat the pre- and post-contrast images as two separate channels of the same data set. This enables joint processing on the resulting multi-spectral volume. (*ii*) For improved bias correction, we have developed a specialized optimization constraint that minimizes the intensity difference between the pre- and post-contrast images in the contrast-free areas. (*iii*) We use the probability map of the “contrast” class, obtained as one of the results of the applied bias correction, as the vessel enhanced image. (*iv*) We developed a multi-atlas-based registration strategy to find anatomical relationship between an unseen WB-MRA vessel tree data and a set of labelled atlas data sets. This association, along with the structured vessel graph, is used to label the vessel tree.

In our work, we focus on the vessels that are clinically important for arterial diseases (Hansen et al., 2007). The list of vessels is presented in Table 1.

An overview of our method is presented in Fig. 1.

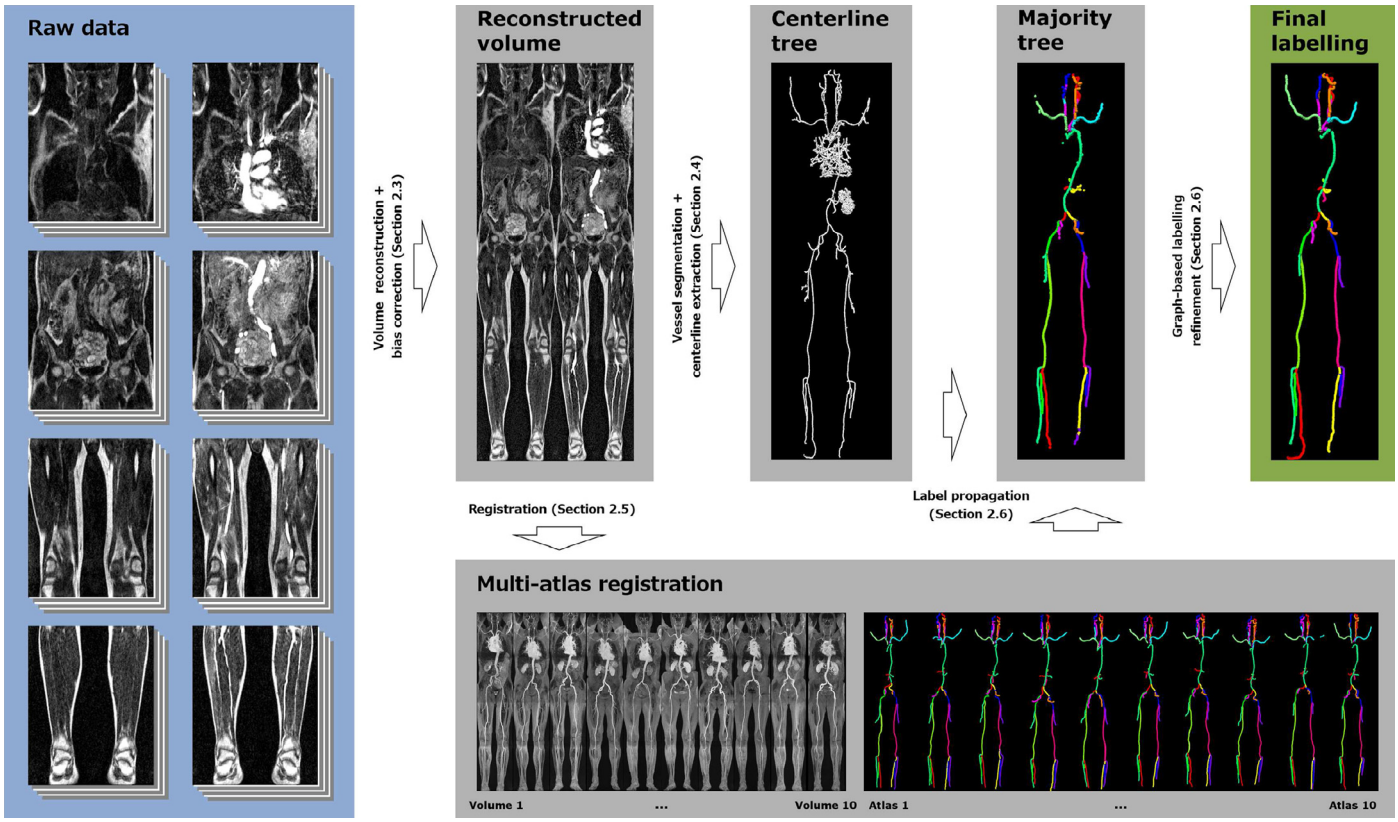

Fig. 1. An overview of our complete automatic pipeline. Detailed description of each step is provided in the corresponding section.

2. Method

2.1. Data

Thirty-five subjects (15 female and 20 male, on average 70 years old) randomly selected from a population-based cohort (Lind et al., 2005) were included in our study. The WB-MRA examination was performed with the standard quadrature body coil on a 1.5T Gyroscan Intera scanner (Philips Medical Systems, Best, The Netherlands). The subject was placed in the supine position, feet-first, on the table, to which an extension of the table top was attached allowing for larger coverage.

The WB-MRA examination was divided into four stations. The first station included the supra-aortic arteries and the thoracic aorta. The second station contained the abdominal aorta, including the renal arteries. Breath-holding was performed for this station. The third station covered the region between the external iliac arteries and the popliteal arteries. The last, fourth, station continued for a varying distance below the ankle. Both pre- and post-contrast T_1-weighted MR scans were acquired. Detailed description about the scan parameters can be obtained from the work of Hansen et al. (2007).

A 3D RF-spoiled T_1-weighted gradient echo acquisition was performed at these four stations, beginning with the fourth station, before the injection. The scan time for each station was 17 s. The table top was moved automatically with the table. The scan time for the pre-contrast images was 87 s, including instructions for breath-holding and table movement, which took 4 s each for the three movements. Thereafter, 40 mL of gadodiamide (Omniscan; GE Healthcare, Oslo, Norway) was injected intravenously with an automated injector (MR Spectris; Medrad, Pittsburgh, PA) at a rate of 0.6 mL/s in 67 s and flushed with 20 mL of saline solution. The scan was set to start after the time defined following the test bolus examination. The stations were scanned in reversed order during the contrast administration, starting with the first station. Another 87 s is required for the following acquisitions for the four stations including table top movement.

The sequence parameters were: TR/TE/flip angle 2.5 ms/0.94 ms/30°; bandwidth 781.3 Hz/pixel; matrix size 256 × 256; number of slices = 60; slices thickness = 4 mm; 80% scan percentage. The acquired voxel size was 1.76 × 1.76 × 4.0 mm^3, which was reconstructed by zero-filling to 0.88 × 0.88 × 2.0 mm^3. Overlap between consecutive stations in the feet-head direction was 30 mm. Linear *k*-space sampling was used for the first station. For the other stations, a method of randomly segmented centric view order (Centra; Philips Medical Systems, Best, The Netherlands) was used.

The 35 WB-MRA data sets were divided into a training set and a test set. A total of 10 WB-MRA scans were selected to be used as the training set and the remaining 25 as the test set. The criteria for selection of the training set were: (*i*) good image quality (few distortions, artefacts, etc.); (*ii*) no missing vessels (due to blockages, fold-over artefacts, motion, etc.); (*iii*) representative scans over the population (different heights, weights, etc.).

2.2. Ground truth vessel tree labels

A semi-automatic tool, called LAVA (De Koning et al., 2003) was used to generate the ground truth centerline vessel trees for each of the 35 WB-MRA scans. The tool requires an observer to manually define the start and the end points of the vessel segment on a maximum intensity projection (MIP) image. The tool then computes a minimum-cost path line between the two points. Since our data sets originate from a population of elderly subjects, a few vessel segments were constricted due to stenosis. For such cases, additional start and end points were required (just before and after the stenotic region) to extract the complete vessel centerline.

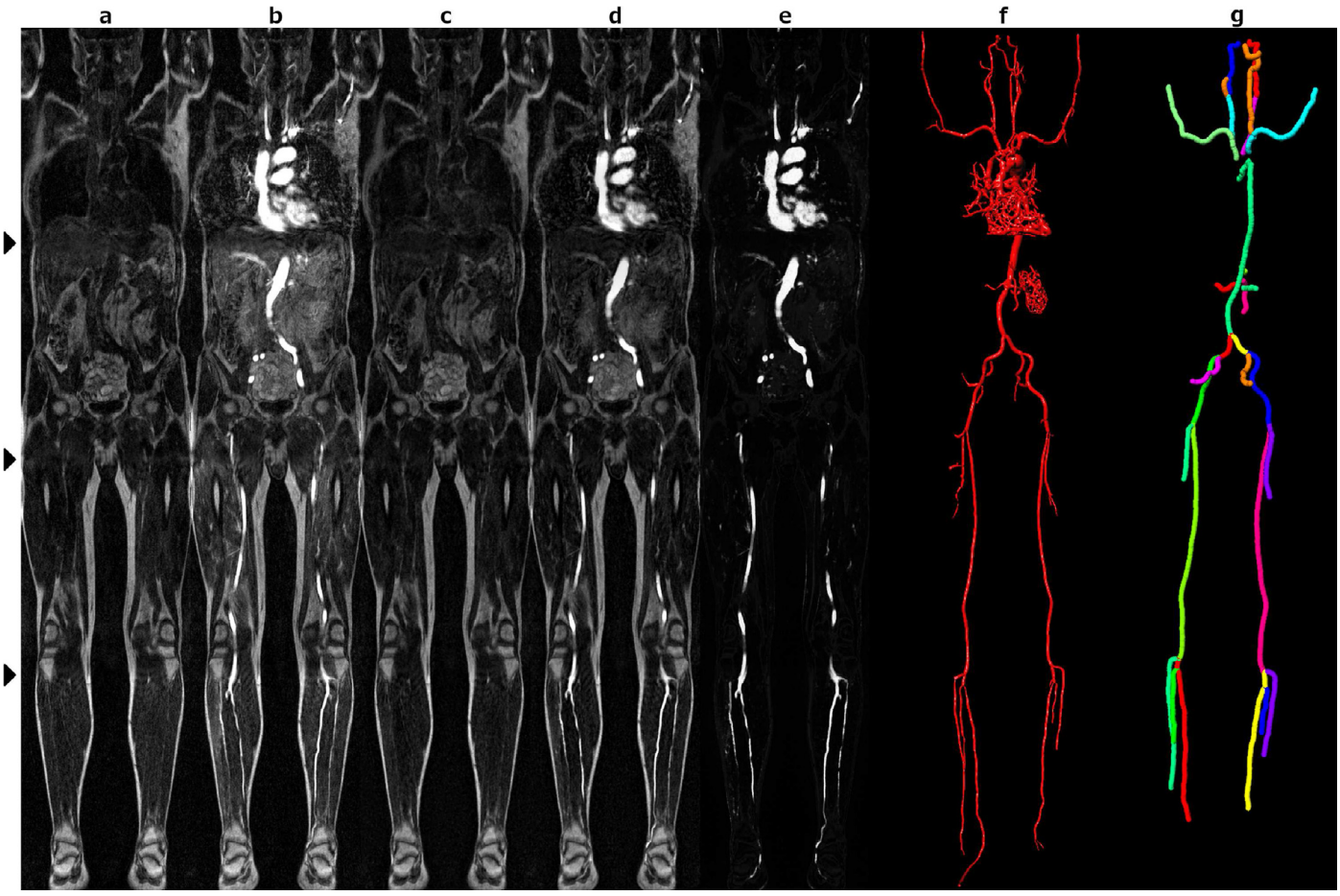

Fig. 2. From left to right: reconstructed pre- (**a**,**c**) and post-contrast (**b**,**d**) WB-MRA volume before (**a**,**b**) and after (**c**,**d**) correction; estimated probability map of the "contrast" class (on the bias-corrected images) (**e**); 3D reconstruction of the final extraction (**f**). Vertical locations of transition lines between different stations are marked by triangles. Labelled centerline tree used as ground truth, different colours represent different vessel segments (**g**). Note that images (**a**)–(**e**) represent one slice from a 3D volume, thus image details, present in different slices, might appear missing in this view. For interpretation of the references to colour in this figure legend, the reader is referred to the web version of this article.

For each of the data sets, vessel centerlines for 32 segments were generated. Each vessel segment also received a label. Left and right branches were assigned separate labels. Femoral+popliteal arteries and subclavian+axillary arteries were assigned one label, due to the lack of a physical branching point between them. A complete list of the vessel segments along with the assigned labels is presented in Table 1.

2.3. Volume reconstruction with intensity inhomogeneity correction

For reconstruction of the complete volume, we used a similar approach to the one described in our earlier work (Dzyubachyk et al., 2013).

In the mentioned work, each reconstructed volume was initially corrected for inter- and intra-station intensity homogeneity, where all the processing is applied jointly to all image channels. After that, all the acquired stations are combined into a single volume. Fig. 2 illustrates a typical WB-MRA volume, before and after the intensity inhomogeneity correction.

The underlying idea of the presented approach is that we treat both pre- and post-contrast images as two separate data channels. This allows us to apply the approach presented in Dzyubachyk et al. (2013), which, however, requires introduction of several important changes to be able to cope with complexity of WB-MRA data. Namely, the registration between the joint intensity histograms corresponding to different stations is reduced to scaling along the "contrast" direction, and novel optimization constraint, reducing difference between pre- and post-contrast images, is developed. The remainder of this section describes our intensity inhomogeneity correction algorithm for WB-MRA images in full detail.

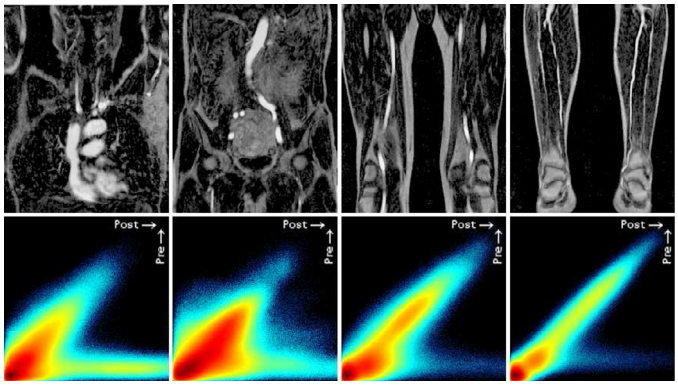

Fig. 3. Joint intensity histograms corresponding to different anatomical regions (stations): (1) head and torso, (2) abdomen, (3) upper legs, and (4) lower legs.

2.3.1. Constrained joint bias correction of pre- and post-contrast images

Fig. 3 illustrates typical joint intensity histograms corresponding to different anatomical regions. Following our approach presented earlier (Dzyubachyk et al., 2013), we define $N = 4$ classes on the joint

intensity histogram. Three of them ($i = \{1, 2, 3\}$), labelled for convenience as "air", "lean tissue", and "fat", are present in both channels, thus the corresponding clusters are located along the diagonal of the joint intensity histogram. The remaining class ($i = 4$), "contrast", is present in one channel only, thus the corresponding cluster is located parallel to the post-contrast axis.

A smooth bias field $\mathbf{b} = (b_1, b_2)$ is iteratively estimated within the fuzzy-c-means-clustering framework by minimizing the following energy functional

$$\mathcal{J}(U, \mathbf{I}, \mathbf{c}, \mathbf{b}) = \int \sum_{i=1}^{N} u_i^q(\mathbf{y}) d_i(\mathbf{y}; \mathbf{I}, \mathbf{c}_i, \mathbf{b}) d\mathbf{y}, \tag{1}$$

where

$$d_i(\mathbf{y}; \mathbf{I}, \mathbf{c}_i, \mathbf{b}) = \int K(\mathbf{x} - \mathbf{y}) \times [(\mathbf{I}(\mathbf{y}) - \mathbf{b}(\mathbf{x}) - \mathbf{c}_i)^T \Sigma_i^{-1} (\mathbf{I}(\mathbf{y}) - \mathbf{b}(\mathbf{x}) - \mathbf{c}_i)] d\mathbf{x},$$

$\mathbf{I} = (I_1, I_2)$ is the image intensity on pre- and post-contrast channels respectively; u_i is the membership probability function of each class; $\mathbf{c}_i = (c_{1,i}, c_{2,i})$ and Σ_i are the center and the covariance matrix of the corresponding cluster; K is a truncated Gaussian kernel that ensures smoothness of the estimated bias field; q is the fuzzifier, in this work the fixed value $q = 2$ was used; and $\mathbf{x}$ and $\mathbf{y}$ are Cartesian coordinates.

Our bias correction algorithm is initialized by calculating the joint intensity histogram and segmenting on it the regions corresponding to each of the four defined tissue classes. Consecutively, the centers $\mathbf{c}_i$ and the covariance matrices Σ_i of each cluster are calculated. These values are kept fixed throughout the entire iterative process as they were very close to the real values.

The membership probability functions of each class are updated during each iteration according to the following formula

$$\widehat{u}_i = \frac{1}{\sum_{k=1}^{N} \left(\frac{d_i}{d_k}\right)^{\frac{1}{q-1}}}. \tag{2}$$

Note, that in this work the classification problem was formulated in the probabilistic manner, whereas in Dzyubachyk et al. (2013) the possibilistic approach was used.

The updated bias field $\widehat{\mathbf{b}}$ is obtained as solution of the linear system of equations

$$\widehat{\mathbf{b}} = \mathbf{J}^{-1} \left(\sum_{i=1}^{N} \Sigma_i^{-1} K * \left(u_i^q (\mathbf{I} - \mathbf{c}_i) \right) \right), \tag{3}$$

with

$$\mathbf{J} = \sum_{i=1}^{N} \Sigma_i^{-1} K * u_i^q.$$

2.3.2. Inter-station intensity inhomogeneity correction

Intensity standardization (Madabhushi and Udupa, 2005) for different stations belonging to the same data set is applied prior to the bias correction described above. In Dzyubachyk et al. (2013) this process is also referred to as "intensity calibration" and is achieved by performing image registration on the joint histograms and consecutive intensity mapping. For the WB-MRA data, such approach cannot be applied due to low similarity between the joint histograms corresponding to different stations as illustrated in Fig. 3. In particular, one can observe severe intensity difference of the contrast material between the stations, caused by the multi-station nature of acquisition as well as the difference in time needed for the contrast to arrive at the particular location. Since the difference in intensity scaling along the "pre-contrast" axis is much less pronounced, we limited ourselves to re-scaling the intensity along the "post-contrast" direction. For that, we have developed an algorithm that consists of the following steps:

1. "Contrast" voxels on each station $s \in \{1, 2, 3, 4\}$ are estimated by applying a triangle threshold t_s on the intensity histogram of the difference image
$$D_s(\mathbf{x}) = I_{2,s}(\mathbf{x}) - I_{1,s}(\mathbf{x}). \tag{4}$$
2. For each station, the mean intensity $\overline{D}_s = mean(D_s(\mathbf{x}))$ of the estimated "contrast" voxels $\mathbf{x} \in \{\mathbf{y}: D_s(\mathbf{y}) > t_s\}$ is calculated.
3. The intensity values of the post-contrast channel are scaled using the regularized Heaviside function
$$H(\mathbf{x}) = 0.5 + \frac{\arctan(\mathbf{x}/5)}{\pi} \tag{5}$$
in such a way that mean intensities of all the stations become equal to the maximal calculated mean
$$I_{2,s}(\mathbf{x}) \mapsto I_{1,s}(\mathbf{x}) + \left[1 + \left(\frac{\max(\overline{D}_s)}{\overline{D}_s} - 1\right) H(D_s(\mathbf{x}) - t_s)\right] D_s(\mathbf{x}). \tag{6}$$

Although the described intensity scaling is rather rough, it is sufficient to be used as an initial approximation for the bias-correction procedure. As result of this step, all the intensities will be refined to become more homogeneous through all the stations as well as within each individual station.

2.3.3. Optimization constraint

Estimation of the bias field can be further improved by providing additional knowledge into the system. Namely, we can assume that real pre- and post-contrast intensity values for the first three, non-contrast, classes are equal. This information can be added to the energy minimization framework in the form of an optimization constraint

$$\begin{aligned} \mathcal{J}_{constr} &= \mathcal{J} + \lambda(\mathbf{x})[(K * \mathbf{I}_2(\mathbf{x}) - \mathbf{b}_2(\mathbf{x})) - (K * \mathbf{I}_1(\mathbf{x}) - \mathbf{b}_1(\mathbf{x}))] \\ &= \mathcal{J} + \lambda \mathbf{A}(K * \mathbf{I} - \mathbf{b}), \end{aligned}$$

for

$$\mathbf{x} \in \{\mathbf{x} : \arg\max_i(u_i(\mathbf{x})) < 4\},$$

where $\lambda = \lambda(\mathbf{x})$ is the Lagrange multiplier (Bertsekas, 1996) and $\mathbf{A} = (-1, 1)$.

The following solution for the Lagrange multiplier λ can be obtained

$$\lambda = \mathbf{A}(K * \mathbf{I} - \widehat{\mathbf{b}}) \left(\mathbf{A}\mathbf{J}^{-1}\mathbf{A}\right)^{-1}, \tag{7}$$

where the expressions for $\widehat{\mathbf{b}}$ and $\mathbf{J}$ are given in (3). The final expression for the bias field in case of the constrained optimization is sobtained by substituting (7) into

$$\widehat{\mathbf{b}}_{constr} = \widehat{\mathbf{b}} + \lambda \mathbf{J}^{-1} \mathbf{A}. \tag{8}$$

2.4. Automated extraction of the vascular tree

A multi-scale vesselness filter (Frangi et al., 1998) was applied on the estimated probability map of the "contrast" class. The scales of the vesselness measures were selected such that only tubular structures with a predefined radius, between the range of 0.5–15 mm, are enhanced. A region growing segmentation using a 3D 26-neighbour relation was initialized to obtain the vessel segmentation. Using prior information about the dimensionality of the scan, the highest intensity voxel in the abdomen (which is located within the aorta) was automatically selected as the seed point for region growing. A typical segmented result is shown in Fig. 2f. Subsequently, the vascular tree $\mathcal{V} = \{\mathbf{v}_{j=\{1,\ldots,n\}}\}$, represented by a set of spatial points $\mathbf{v}_j$, was extracted by skeletonizing the vessel segmentation result by applying a homotopic thinning algorithm (Pudney, 1998).

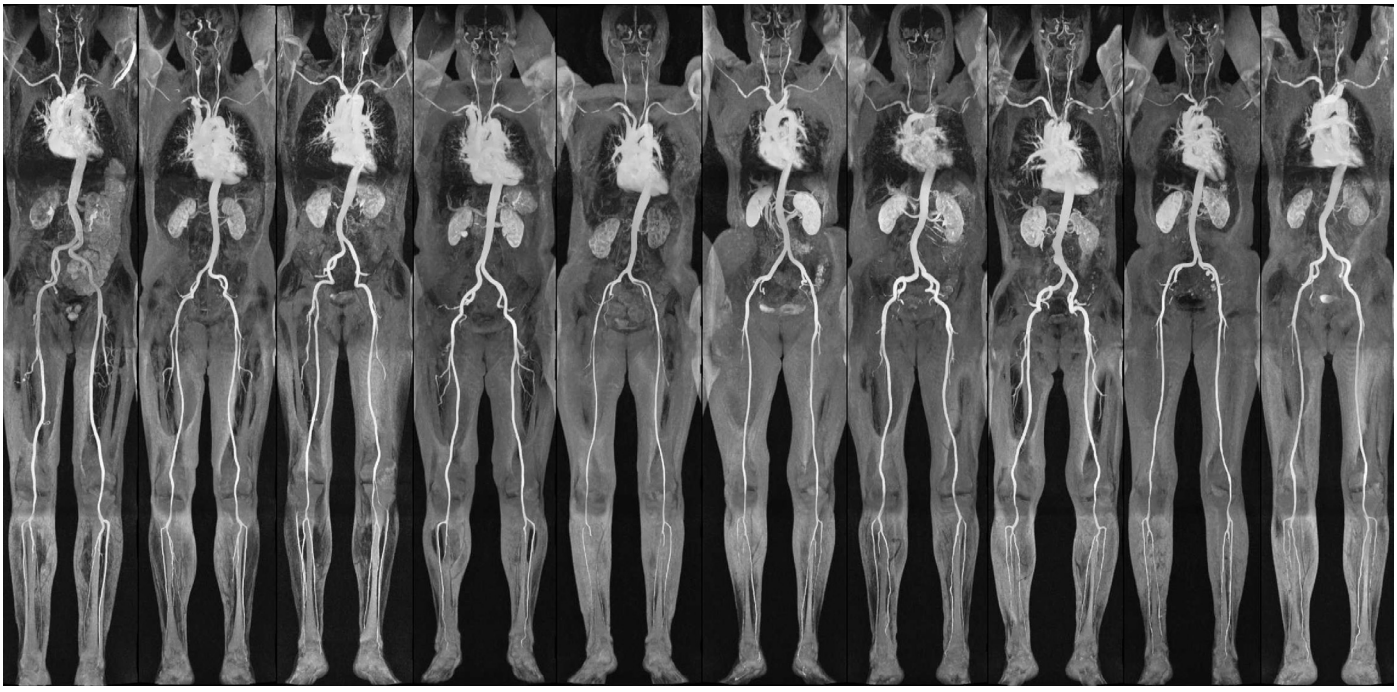

Fig. 4. Different atlas images used, displayed here in their MIP form. It can be noted the variation of the vascular tree between the atlases.

2.5. Multi-atlas based registration

Image-based registration is used to obtain anatomical correspondence between a labelled WB-MRA atlas scan (A) and an unseen WB-MRA subject scan (S) (Suri et al., 2007). In the registration procedure, the transformation parameters T that minimize the cost function $C(T; A, S)$ between the fixed image (A) and a moving image (S) are determined. The optimization problem can be mathematically represented as

$$\hat{T} = \arg\min_{T} C(T; A, S). \tag{9}$$

Detailed information on atlas registration is provided elsewhere (Rohlfing et al., 2005). The resulting transformation T from the registration is used to map a set of labelled points from the atlas scan (A) onto the subject scan (S).

In our work, we use 10 atlases, such that the anatomical variations between the subjects are better represented (Aljabar et al., 2009; van Rikxoort et al., 2010), as visualized in Fig. 4. The 10 training data sets were used as atlas scans. The atlases consist of vessel centerlines for each of the 32 segments (see Table 1). After the registration, the labelled centerline points are propagated from A to S.

We investigated various registration strategies with different scan types (pre-, post-contrast, vesselness, etc.), different cost functions (C), and also multi-stage approaches. Section 3.2 explains this step in full detail.

2.6. Vascular tree labelling

Our graph labelling algorithm returns a complete labelled vascular tree using the corresponding extracted tree $\mathcal{V}$ and 10 registered atlases as inputs. The labelling is done in two stages: (i) initial labelling on a point level, using the label propagation from the registered atlases; and (ii) final labelling by using the structure information of the extracted vessel tree.

For obtaining initial labels, the labelled trees from the atlas scans are used. This is done by mapping each of the atlas centerline trees onto the subject scan, using the registration approach explained is Section 2.5. Then, for each point $\mathbf{v} \in \mathcal{V}$ of the subject's tree, the nearest point $\mathbf{a}_j$ from each of the mapped atlas trees $\mathcal{A}_{j\in\{1,\ldots,10\}} = \{\mathbf{a}_j\}$, is calculated. At this point we disregard all the points $\mathbf{a}_j$ located further than the empirically defined threshold of 5 mm away from $\mathbf{v}$ (here we use the Euclidean distance). This results in the following set of labels $L_A(\mathbf{v}) = \left\{L(\mathbf{a}_j) : \|\mathbf{a}_j - \mathbf{v}\| \leq 5\right\}$, which can contain from zero to ten entries. Next, we perform majority voting on $L_A(\mathbf{v})$, resulting in the set $L_A^{maj}(\mathbf{v}) = \left\{L^{maj} : L^{maj} = \arg\max L(\mathbf{a}_j)\right\}$ containing all entries of the most probable label L^{maj} for the given point. Finally, the majority label $L^{init}(\mathbf{v}) = L^{maj}$ is assigned to the point $\mathbf{v}$ if the set $L_A^{maj}(\mathbf{v})$ contains at least two elements: $|L_A^{maj}(\mathbf{v})| \geq 2$, otherwise its label remains zero.

Such label propagation typically produces a result that contains errors of several types (gaps in the labelled tree, label swaps, incompletely labelled segments, etc.) due to the varying anatomy of the vascular structures. Thus, in the second stage, the obtained initial labelling is refined by using the structure information of the extracted tree $\mathcal{V}$. Here we represented $\mathcal{V}$ by a graph $\mathcal{G} = \langle N, E\rangle$, where nodes N represent the bifurcations and end points of the vessel tree, and edges E, consisting of a set of associated points, connect two nodes. The labelling is refined using the following steps:

1. Initially, each edge E of the extracted graph $\mathcal{G}$ is labelled according to the majority voting on the labels initially assigned to its points: $L = \arg\max \left\{L^{init}(\mathbf{v}) : \mathbf{v} \in E\right\}$. Along with the label L, its "weight" $w(E, L)$, equal to the number of the edge points that initially got labelled, is recorded: $w(E, L) = \left|\left\{\mathbf{v} \in E : L^{init}(\mathbf{v}) > 0\right\}\right|$. Similar, the normalized weight of the label L is defined as $n(E, L) = w(E, L)/\sum_{\mathcal{G}} w(:, L)$.
2. Next, a minimum connected graph spanning the labelled edges is calculated. Some of the unlabelled edges might also be included in the graph at this point to keep it connected. Each of these edges is assigned the label of the neighbouring edge with the largest weight $w(E, L)$. In case the connected spanning graph cannot be created because its parts are disjoint, those are connected with an "artificial" edge connecting closest nodes of two separated parts. Such "artificial" edges contain no points. The nodes and the edges

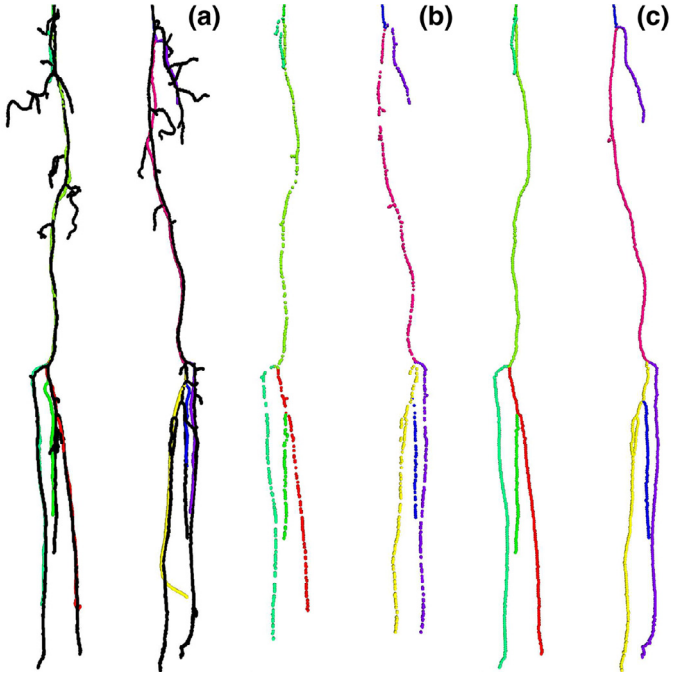

Fig. 5. Overview of the labelling steps. (**a**) Mapped centerline tree, black points represent subject's unlabelled tree and the coloured points are the centerline segments from one of the atlas scans. (**b**) Majority voted centerline points of the subject. (**c**) Final labelled graph tree. For visual clarity only the leg area is shown. For interpretation of the references to colour in this figure legend, the reader is referred to the web version of this article.

that are not part of the created minimum connected spanning graph are removed.

3. Next, we prune the obtained graph by repeating two following steps until no further pruning is possible:
   (a) All nodes having degree (number of adjacent edges) of 2 are removed and the adjacent edges are combined into a single edge. The label weights $w(E, L)$ of the resulting edge are updated accordingly.
   (b) For all nodes with degree ≥ 3, the "side" (removing which will not make the graph disjoint) edges E are pruned if $n(E, L) < 0.2$. Note, that this rule is designed in such a way that all the branches satisfying this condition are removed. In practice, however, we did not encounter cases when more than one branch was removed at a time.
4. Finally, the resulting pruned graph is labelled within two-stage process:
   (a) For each of the present labels, one edge is labelled by running the Hungarian algorithm of Kuhn (1955) on the normalized label weights matrix **n**. The weights whose probability for the given segment is less than 0.05 were set to zero beforehand.
   (b) Next, all the remaining edges E are given the label with the maximum weight $w(E, L)$.

A visual overview of all the labelling steps is shown in Fig. 5.

3. Experiments and results

We perform four types of experiments to evaluate the proposed method. (*i*) We investigate the accuracy of the centerline extraction step on the entire set of 35 WB-MRA scans (see Section 3.1). (*ii*) We investigate the performance of our bias correction and volume reconstruction approach in comparison with the traditional digital subtraction angiography (DSA) on the 35 WB-MRA data sets (see Section 3.1). (*iii*) We perform leave-one-out analysis on the training set to investigate various registration strategies (see Section 3.2). (*iv*) We investigate the performance of our complete method on the test set by comparing the accuracy of the automatically generated vessel segments to those obtained manually (see Section 3.3).

Table 2
Results of the visual validation of the arterial tree extraction and comparison of our proposed method to the conventional DSA approach.

Detection (%)	Our method	Subtraction angiography
Complete segment	82.4	77.5
Partial segment	11.7	8.3
Missed segment	5.9	14.4
Leaked into non-vessel	6.8	10.3
Leaked into vessel	7.6	24.0

3.1. Visual validation

Visual analysis was performed on the segmented vessels (as described in Section 2.4). A trained medical student graded a vessel segment as completely extracted, partially extracted, or missed all together. The observer also checked if the vessel of interest abnormally merged (leaked) into surrounding vessels or other structures. The vessel tree was divided into 32 vessel segments as presented in Table 1. The right and left branches were evaluated separately.

Table 2 presents the findings from the visual validation on 1120 segments from 35 subjects. On average, per subject out of the 32 segments, 28 were detected, 2 were partially detected, and 2 missed. The aorta, brachiocephalic trunk, iliac arteries, femoral arteries, and popliteal arteries were detected in all subjects. The partially detected and missed segments were usually the smaller vessels or the carotid arteries. It was also noted that there were 37 segments with cases of peripheral arterial stenosis in our data set.

We conducted an additional experiment where we repeated the visual validation, but this time the vessel segmentation was obtained using DSA. We first stitch the scans from the four stations to generate the WB-MRA volumes for the pre-contrast and post-contrast MR scans, then co-register the two scans in order to remove any motion that was introduced between the two examinations, and finally digitally subtract the two scans. The vessels are segmented using region growing on the vesselness image (as explained in Section 2.4) of the subtraction angiography image. The results of the analysis are presented in Table 2.

3.2. Leave-one-out analysis

We performed a number of experiments to optimize the registration parameters and to select the best approach that results in the highest accuracy. Leave-one-out analysis was performed only on the training set. All registrations were performed using `elastix` (Klein et al., 2010), a package for medical image registration publicly available from http://elastix.isi.uu.nl.

The accuracy of the registration step was evaluated by comparing a set of 21 landmark points placed at identifiable anatomical locations along the arterial tree. The location and the number of the landmarks are shown in Table 3.

Images in various forms were used in the registration step: post-contrast WB-MRA scan (MRA), vesselness scan (VESS), Euclidean distance transformed vesselness scan (EDTF).

The similarity measures investigated were: mutual information (MI), normalized cross correlation (NCC), and sum of squared differences (SSD).

We investigate the registration performance on various combinations of scan types and similarity measures, also multi-stage approaches were investigated. Fig. 6 shows the comparison of the various registration strategies. Accuracy is measured using the sum

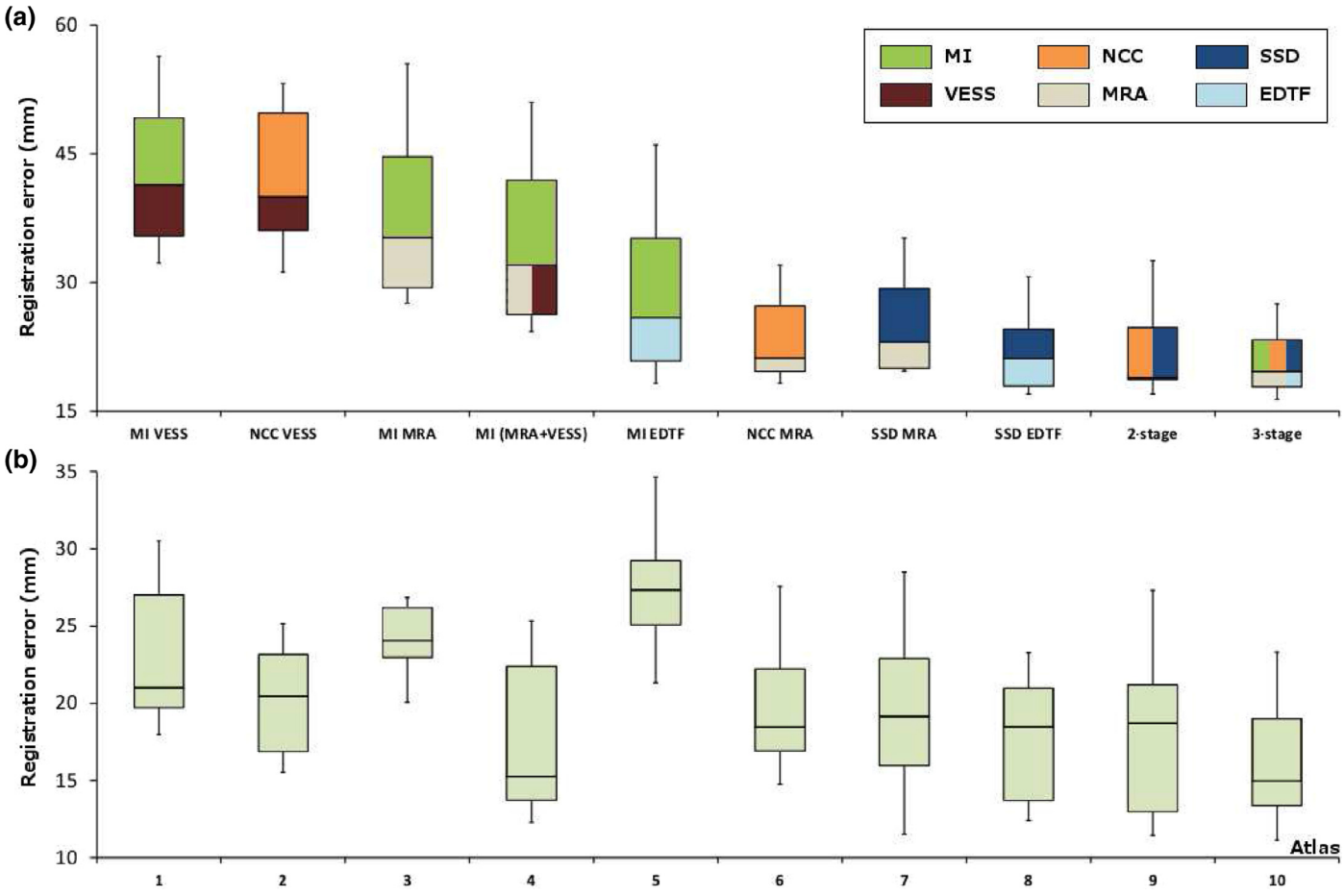

Fig. 6. (**a**) Results of the registration accuracy using different strategies. Here the registration error is defined as the residual Euclidean distance calculated over all landmarks. Different colors in the box plots indicate the different image types and different cost functions used. (**b**) Leave-one-out analysis on each of the 10 atlases using "3-stage" registration strategy. For interpretation of the references to colour in this figure legend, the reader is referred to the web version of this article.

Table 3
Set of landmark points used to validate the registration accuracy. The landmark points are placed at anatomically relevant locations along the arterial tree.

Anatomical location	Number
Bifurcation: internal and external carotid's	2
Base of common carotid arteries	2
Aortic arch	1
Bifurcation: aorta and renal arteries	1
Bifurcation: aorta and common iliac arteries	1
Bifurcation: internal and external iliac arteries	2
Bifurcation: common and deep femoral arteries	2
Bifurcation: tibial artery	2
Bifurcation: fibular artery	2
Bifurcation: popliteal and tibial artery	2
Base of vertebral artery	2
Base of axillary artery	2

of Euclidean distances over the 21 defined landmark points, using a leave-one-out strategy.

1. **MI VESS**: The registration was performed on the VESS scans using MI, in two stages. Initially, an affine transformation was applied to roughly align the atlas and subject scans. This is followed by a B-spline transformation, using the result of the affine registration as initialization. A multi-resolution approach is used in both stages. The registration process starts with images that have lower level of detail and continues with higher resolution images. This is repeated up to the original image resolution. In our strategy, we used up to three resolutions. A powers-of-2 pyramid schedule (which defines the amount of blurring and down-sampling for each resolution level) is used.
2. **NCC VESS**: Similar strategy as mentioned above is used here, except that the similarity measure is NCC.
3. **MI MRA**: Uses the same strategy as MI VESS, but the registrations are performed on the MRA scans instead of the VESS scans.
4. **MI** (MRA+VESS): In this registration strategy, we used information from two different scan types: MRA and VESS. Basically, we combine the MI MRA and MI VESS strategies. We begin with the MI MRA registration stage (affine + B-spline), the resulting transformation from this stage is used to drive the B-spline transformation in the MI VESS registration.
5. **MI EDTF**: Uses the same strategy as before, but on EDTF scans using MI.
6. **NCC MRA**: Similar to NCC VESS, but on MRA scans.
7. **SSD MRA**: Similar to NCC MRA, but using SSD.
8. **SSD EDTF**: Similar to SSD MRA, but on EDTF scans.
9. **2-stage**: Similar to the MI (MRA+VESS) strategy, but here we use different similarity measures on different scan types. We use the result of the NCC MRA stage to initialize the B-spline transformation on an EDTF scan using SSD as the similarity metric.
10. **3-stage**: In this strategy, we combine information from the above strategies. We begin with an affine registration on the MRA scan using MI, followed by a B-spline transformation on

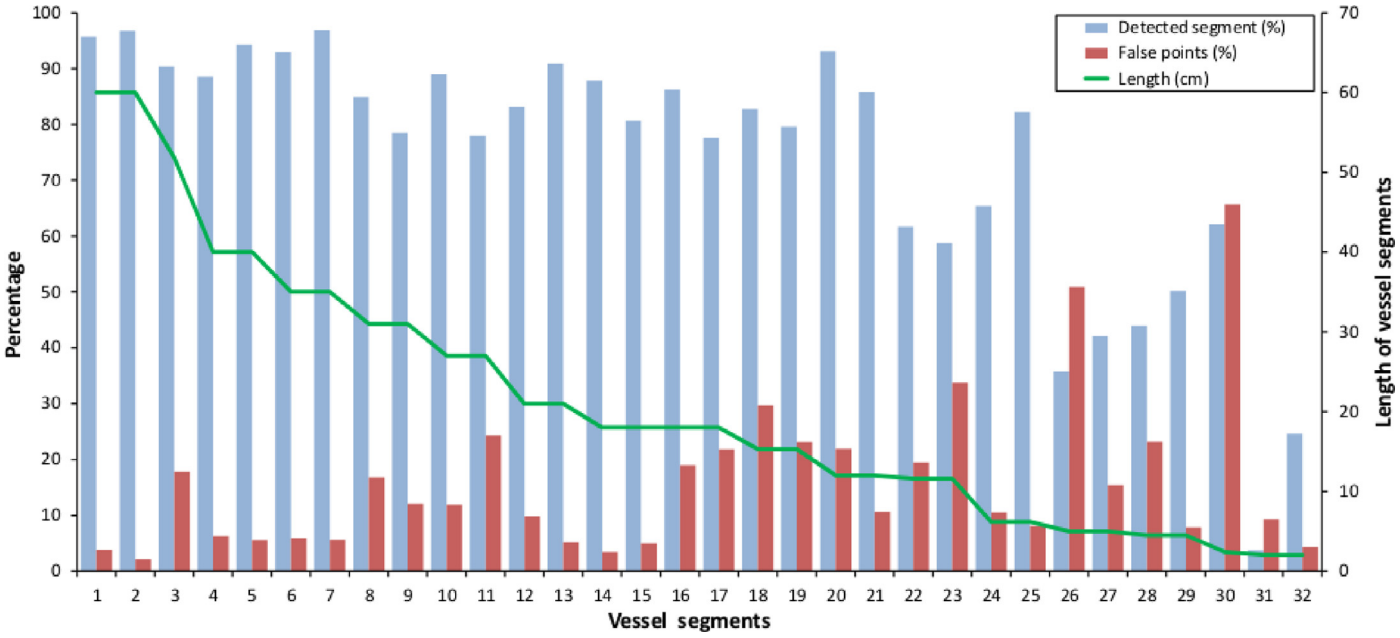

Fig. 7. Average labelling accuracy over the training set for each of the vessel segments. Notice that the accuracy drops as the vessels get shorter.

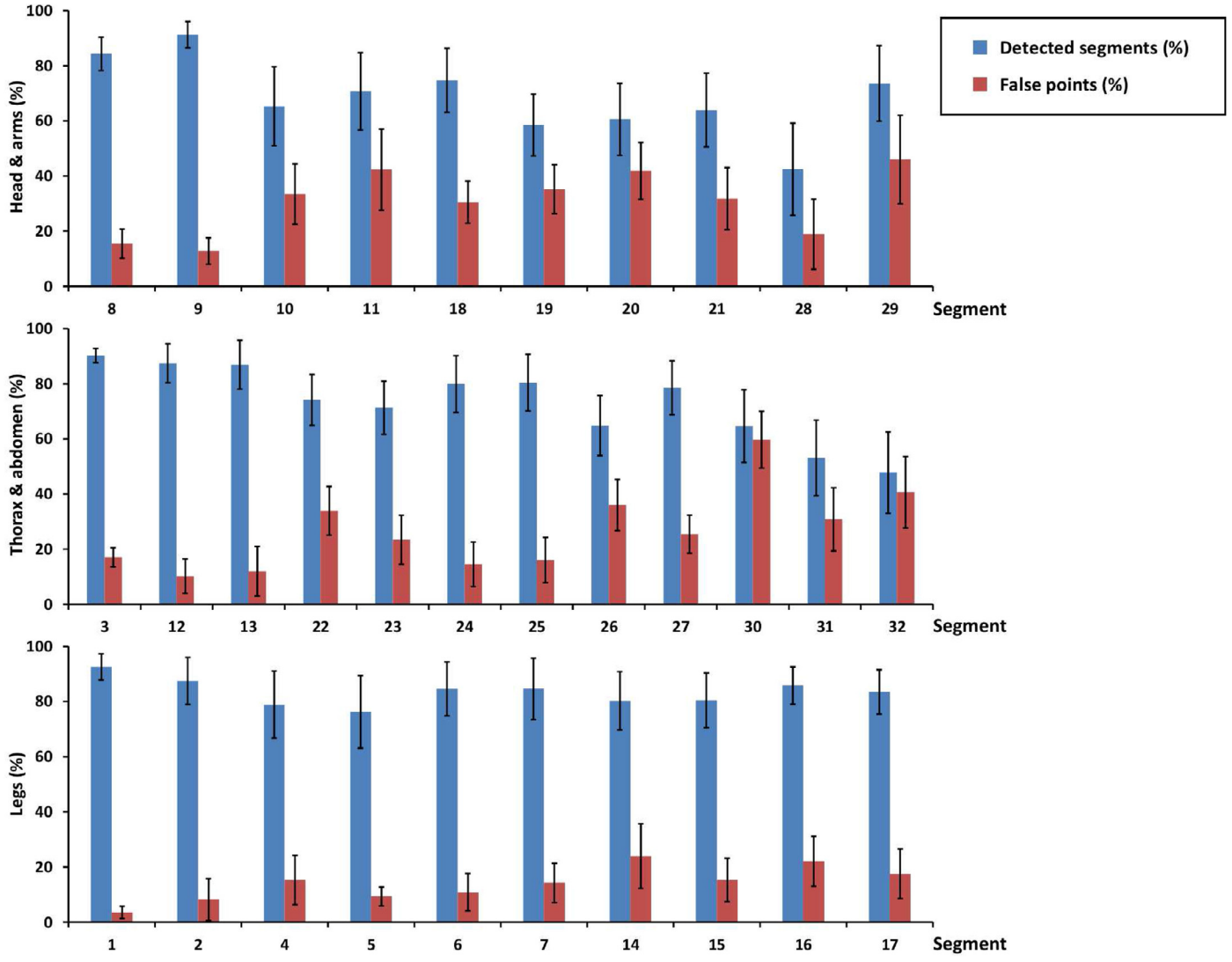

Fig. 8. Average labelling accuracy of our method over the test set for the vessels in the neck and arms (top), thorax and abdomen (middle), and the legs (bottom).

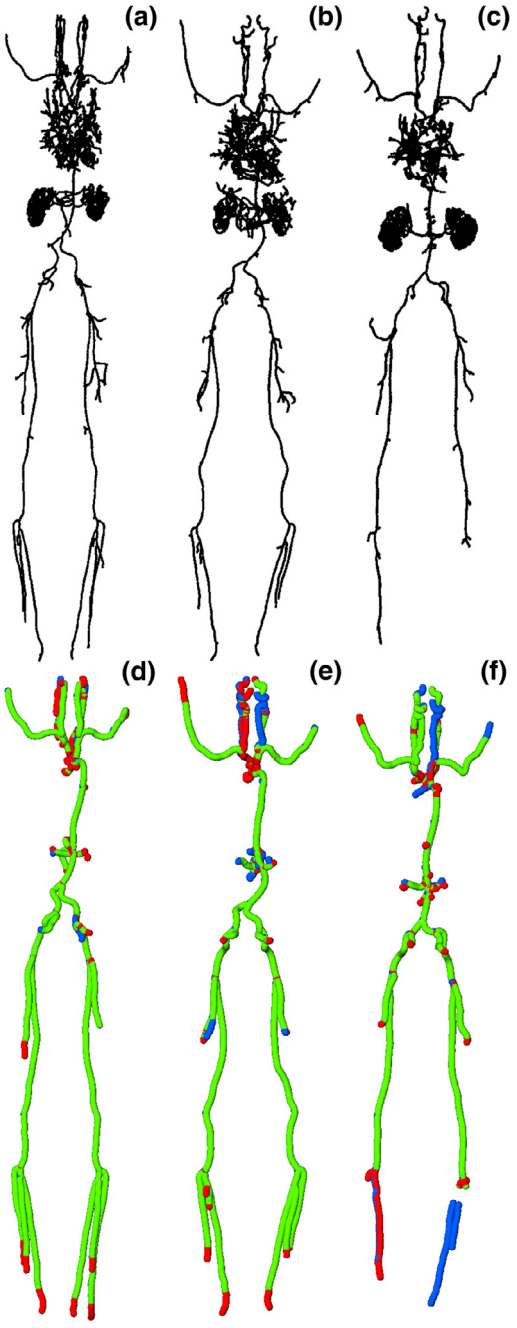

Fig. 9. Sample results of the labelled vessel trees: Images (**a**–**c**) represent the complete extracted vessel tree. Images (**d**–**f**) show the pruned and labelled tree, where green were correctly labelled, blue were missed, and red were falsely detected segments. The three trees correspond to subjects number 23, 16, and 25 in Fig. 10. For interpretation of the references to colour in this figure legend, the reader is referred to the web version of this article.

the MRA scan using NCC, which is, in-turn, followed by another B-spline transformation on EDTF scan using SSD.

It can be observed from the Fig. 6a that the strategy with the best results is the "3-stage" registration approach.

We further investigated the performance of the individual scans from the training set using the "3-stage" registration strategy, the results of which are shown in Fig. 6b. It can be observed that atlas number 5 has the worst performance. Hence, it was removed from the set of atlas scans that were used for the main experiments.

Since our end goal is to investigate the accuracy of the labelled segments, we checked the average labelling accuracy over the remaining 9 atlas images and all the vessel segments. Fig. 7 presents the results of our vessel labelling pipeline.

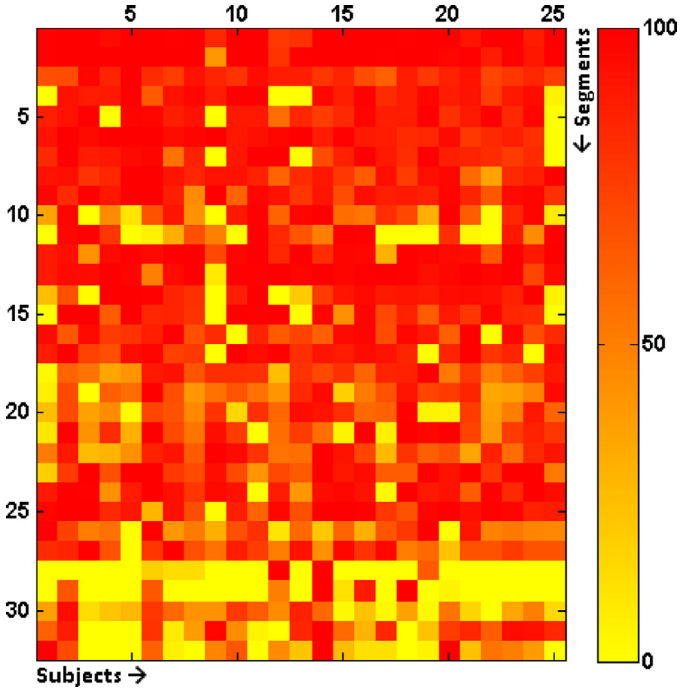

Fig. 10. Detection and labelling accuracy for each of the 32 vessel segments over the entire test set. Segments are ordered according to the average anatomical length, as presented in Table 1.

3.3. Labelling accuracy on the test set

Fig. 8 shows the accuracy of labelling the vessel segments along with the average number of false positive centerline points detected by our method. The results are presented separately for the vessels in the neck and arms, thorax and abdomen, and legs. It can be noticed that the accuracy of the method is very good in the legs and has relatively lower performance in the neck and arms region. Fig. 9 provides several illustrative examples of results of varying quality.

Fig. 10 shows the performance of the detection and labelling accuracy of our pipeline over the test set. The segments have been ordered on the category axis according to the labels in Table 1. It can be noted that errors occur mainly at the bottom of the figure, where the vessels represented are comparatively short.

4. Discussion

A method for automated extraction and labelling of the arterial tree from WB-MRA scans has been proposed and quantitatively evaluated. Our method differs from state-of-the-art approaches for extraction of the entire vessel tree from the WB-MRA images in that we are performing segmentation in full 3D, rather than on the MIP images.

In the experiments, we compared the vessel extraction accuracy using our proposed approach to that of DSA. Our method had a higher detection accuracy and a lower error rate with respect to segments leaking into neighbouring structures. The accuracy of the vessel extraction is enhanced by the prior intensity inhomogeneity correction. In particular, re-scaling the intensity of the "contrast" class between different stations has positive effect on quality of the entire vascular tree extraction, especially around the vessel narrowing. Correction of the bias field, whose strength is typically increasing towards

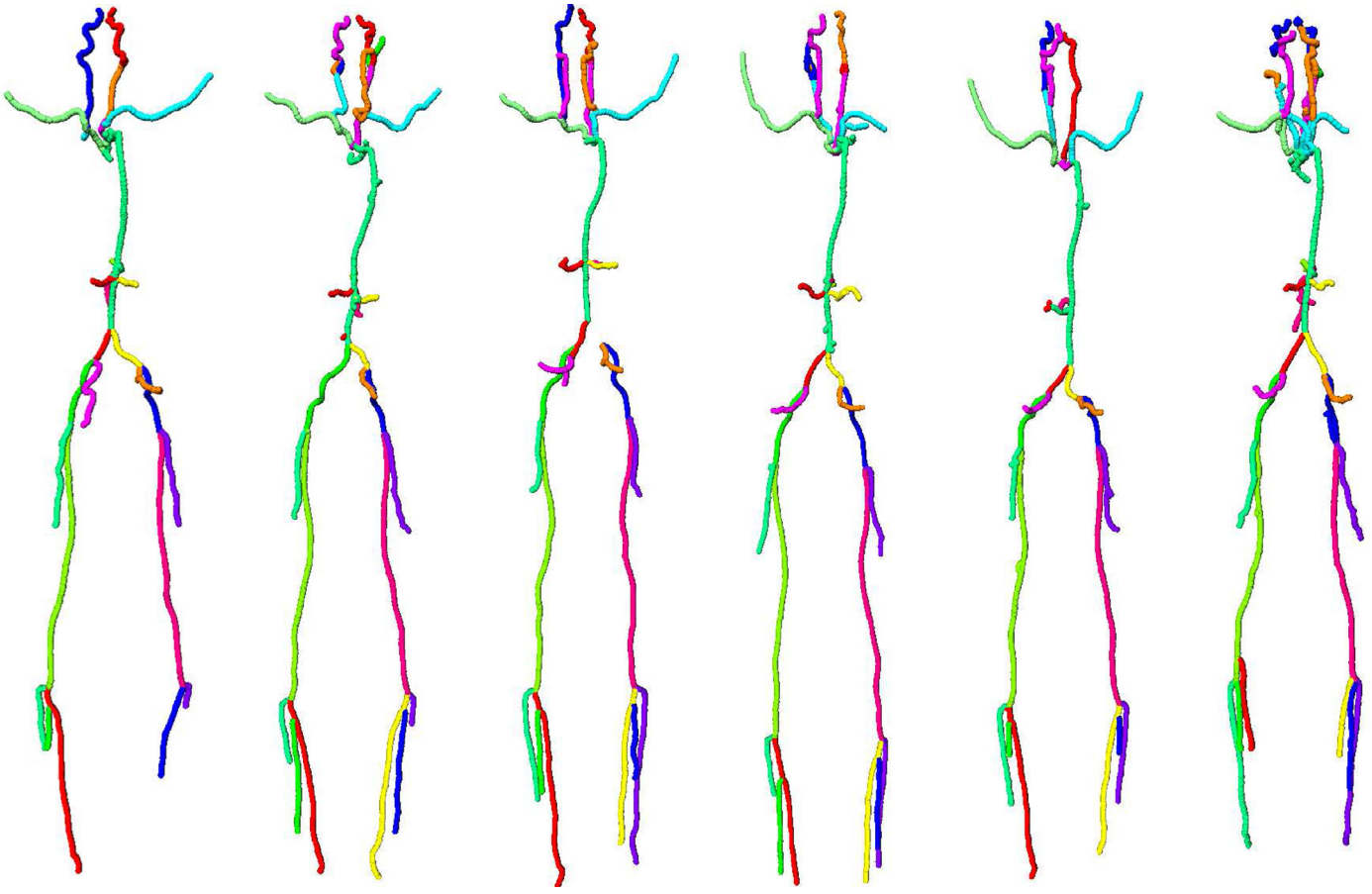

Fig. 11. Examples of completely labelled vessel trees from a number of subjects. Different colors represent different vessel segments. The cases were our method was able to successfully handle the variation in the branching patterns and segment lengths as well as failure cases (missing or incorrect labels) are shown. The examples presented here correspond to subjects number 1, 6, 11, 17, 21, and 23 in Fig. 10.

the edges of each stack, resulted in improved continuity of the vessels between consecutive stacks. Moreover, for the vessel extraction, we suggest using the probability map of the "contrast" class, that, unlike the difference image between the post- and pre-contrast channels, does not suffer from the motion-related artefacts. Comparing the results as presented in Table 2, it can be noted that our proposed method has a superior performance.

The results indicate that our automated extraction and labelling method is very robust. However, the validation was performed on a data set that was rather limited with respect to both number of subjects and presence of large pathological abnormalities. Testing our method on a larger set of clinical data is subject of future research. Fig. 11 shows a few examples of the complete labelled tree. We investigated the performance of our method over 32 different vessel segments over the entire human body. The results obtained show that 82.4% of the vessel segments were completely extracted. The majority of missed segments were located in the neck, especially the external carotid arteries (they could be completely extracted in only 25 subjects) and the vertebral arteries (these could be completely extracted in 18 subjects). These arteries have relatively small diameters and were not clearly visible due to insufficient spatial resolution. The vessels in the neck were further affected by fold-over artefacts. This resulted in some of the carotid artery segmentation leaking into non-vascular regions. The data sets used to validate our method were obtained from a population-based study that included elderly subjects. Several of them had peripheral arterial diseases, resulting in vessel narrowing. There were 37 cases of stenosis in our data sets. Such vessels were partially segmented due to the sudden drop in intensity. These cases were found mainly in the leg region, especially the fibular artery (this segment was partially detected in about 50% of the subjects). The performance of the vessel labelling process can be seen in Figs. 7 and 8. The method performs very well on most of the segments, whereas for vessels that are smaller than 5 cm in length the performance is moderate (see Fig. 7). On the test set (see Fig. 8) it can be observed that there are a few outliers with respect to the labelling accuracy. Generally, the performance is poor in the neck region. As stated previously, it is difficult to accurately segment and label these vessels due to the various imaging artefacts and the low scan resolution. The other outlier, the brachiocephalic trunk, is located in the thorax region. It is typically 4 cm long and connects the aorta to the right common carotid artery and the right subclavian artery. Due to large anatomical variations between the atlases and the subject scans, this small vessel segment is sometimes wrongly labelled. The other two outliers are the superior mesenteric artery and the celiac trunk, these are small vessel segments in the abdomen. These vessels were not always visible due to the scanning protocol. It was also observed that, in general, there were errors in the labels either at the bifurcations or at the end of the vessel segment, especially in the leg region (the red regions in Fig. 9). In reality, these errors were due to inconsistent ground truth labels: the observer had to use a 2D MIP image to place the seed points, which causes visual perception issues. The actual bifurcation point could not be accurately determined on a 2D view. And, due to low contrast at the end of the vessel segment, the observer had to make an educated guess as where the segment stops. This is another reason why performing analysis on MIP images is not very beneficial.

A combination of multi-atlas and graph-based methods used in our method to label the extracted vessel tree has never been

investigated before. In our study, we demonstrated that this combination has very good performance. Making use of anatomical knowledge from a number of atlases to obtain initial labels for the vessel tree is very beneficial. Using only a graph-based approach to label the vessel tree would be computationally very expensive as the underlying graph structure of the whole body is very complex.

We investigated multi-atlas registration by performing a number of experiments (Section 3.2). We looked at three different types of images in our registration experiments: MRA, VESS, and EDTF. The registration error was rather high when using the VESS image, as the registration method could not handle the vessel pattern variations between the subjects. Only the larger vessels were accurately aligned. When the MRA images were used, the registration error was slightly lower compared to the VESS approach. Unlike the VESS images, the MRA scans had much more surrounding tissue information. This extra information helped driving the registrations in the correct direction and could globally align the fixed and the moving images more accurately. However, the vascular structure still had large deviation. The third type of image information used is EDTF, which was obtained by applying the Euclidean distance transform on the VESS image. Using the EDTF image helped the registration to converge much better into the vascular structure, resulting in a lower registration error. In our proposed "3-stage" registration approach, we used both the MRA and EDTF images. First, the MRA images were used to globally align the fixed and moving images. Second, using the initial MRA registration, the EDTF images were used to fine-tune the alignment of the vascular structure.

The ultimate goal of our study in the near future is to be able to perform vessel-specific vascular analysis, i.e. to be able to detect and quantify stenosis and/or aneurysms. In order to perform this task accurately, it is important that the extraction and labelling stages are very robust. A number of lumen segmentation methods that could help us realize this goal already exist. For example, one of our previous methods (Shahzad et al., 2013) can be modified and applied in combination with our proposed method for accurate lumen segmentation and stenosis or aneurysm quantification.

The multi-atlas registration approach is rather sensitive to image quality and scan parameters. One subject (number 9) exhibited some vessel labelling errors, as seen in Fig. 10. Due to poor image quality, majority of the atlas scans failed to converge on a vessel label. This initial labelling error further propagated through the pipeline and caused erroneous vessel labelling.

The results presented in this paper are completely automated. On the other hand, if necessary, limited manual interaction can be easily applied to correct the results of our method. For instance, such interaction can be applied at the extraction stage, where missed vessel segments can be retrieved by placing an extra seed point to facilitate the region growing segmentation. User interaction can also be included to correct for label swaps due to registration inaccuracy.

5. Conclusions

In conclusion, in this work we demonstrated the possibility of fully automated extraction of the entire 3D arterial tree. We also demonstrated the ability to automatically label the arterial tree. With a large number of population-based screening studies being conducted nowadays, it will be of great advantage to have automated methods that can robustly extract and label the vessels for further quantitative analysis. Such as measuring the degree of stenosis or the diameters of aneurysms.

This is the first study where complete automated extraction and labelling of the vascular tree has been investigated. The presented results indicate high potential for future clinical and population-based studies.

Acknowledgments

This research was supported by the Dutch Technology Foundation STW (Stichting Technische Wetenschappen) via Grant 10894 and the Swedish Research Council by Grant 2012–2330.

References

Aljabar, P., Heckemann, R.A., Hammers, A., Hajnal, J.V., Rueckert, D., 2009. Multi-atlas based segmentation of brain images: atlas selection and its effect on accuracy. Neuroimage 46, 726–738.
Bertsekas, D.P., 1996. Constrained Optimization and Lagrange Multiplier Methods. Optimization and neural computation, Athena Scientific. Athena Scientific, Nashua 1 ed.
Bogunović, H., Pozo, J.M., Cárdenes, R., San Román, L., Frangi, A.F., 2013. Anatomical labeling of the circle of Willis using maximum a posteriori probability estimation. IEEE Trans. Med. Imaging 32, 1587–1599.
Börnert, P., Aldefeld, B., 2008. Principles of whole-body continuously-moving-table MRI. J. Magn. Reson. Imaging 28, 1–12.
De Koning, P., Schaap, J., Janssen, J., Westenberg, J., van der Geest, R., Reiber, J., 2003. Automated segmentation and analysis of vascular structures in magnetic resonance angiographic images. Magn. Reson. Med. 50, 1189–1198.
Dzyubachyk, O., van der Geest, R.J., Staring, M., Börnert, P., Reijnierse, M., Bloem, J.L., Lelieveldt, B.P.F., 2013. Joint intensity inhomogeneity correction for whole-body MR data. In: Mori, K., Sakuma, I., Sato, Y., Barillot, C., Navab, N. (Eds.), Medical Image Computing and Computer-Assisted Intervention. Springer, Nagoya, Japan, pp. 106–113.
Flasque, N., Desvignes, M., Constans, J.-M., Revenu, M., 2001. Acquisition, segmentation and tracking of the cerebral vascular tree on 3D magnetic resonance angiography images. Med. Image Anal. 5, 173–183.
Frangi, A.F., Niessen, W.J., Vincken, K.L., Viergever, M.A., 1998. In: Wells, W.M., Colchester, A., Delp, S. (Eds.), Multiscale vessel enhancement filtering. Springer, Cambridge, MA, USA.
Goehde, S.C., Hunold, P., Vogt, F.M., Ajaj, W., Goyen, M., Herborn, C.U., Forsting, M., Debatin, J.F., Ruehm, S.G., 2005. Full-body cardiovascular and tumor MRI for early detection of disease: feasibility and initial experience in 298 subjects. Am. J. Roentgenol. 184, 598–611.
Gülsün, M.A., Funka-Lea, G., Zheng, Y., Eckert, M., 2014. CTA coronary labeling through efficient geodesics between trees using anatomy priors. In: Golland, P., Hata, N., Barillot, C., Hornegger, J., Howe, R. (Eds.), Medical Image Computing and Computer-Assisted Intervention. Springer, Boston, MA, USA, pp. 521–528.
Hameeteman, K., Zuluaga, M.A., Freiman, M., Joskowicz, L., Cuisenaire, O., Valencia, L.F., Gülsün, M.A., Krissian, K., Mille, J., Wong, W.C., et al., 2011. Evaluation framework for carotid bifurcation lumen segmentation and stenosis grading. Med. Image Anal. 15, 477–488.
Hansen, T., Wikström, J., Johansson, L., Lind, L., Ahlström, H., 2007. The prevalence and quantification of atherosclerosis in an elderly population assessed by whole-body magnetic resonance angiography. Arterioscler. Thromb. Vasc. Biol. 27, 649–654.
Isgum, I., Staring, M., Rutten, A., Prokop, M., Viergever, M.A., van Ginneken, B., 2009. Multi-atlas-based segmentation with local decision fusion–application to cardiac and aortic segmentation in CT scans. IEEE Trans. Med. Imaging 28, 1000–1010.
Jäger, F., Hornegger, J., 2009. Nonrigid registration of joint histograms for intensity standardization in magnetic resonance imaging. IEEE Trans. Med. Imaging 28, 137–150.
Klein, S., Staring, M., Murphy, K., Viergever, M.A., Pluim, J.P., 2010. `elastix`: a toolbox for intensity-based medical image registration. IEEE Trans. Med. Imaging 29, 196–205.
Kuhn, H.W., 1955. The Hungarian method for the assignment problem. Nav. Res. Logist. Q. 2 (1–2), 83–97.
Ladd, S.C., Debatin, J.F., Stang, A., Bromen, K., Moebus, S., Nuefer, M., Gizewski, E., Wanke, I., Doerfler, A., Ladd, M.E., et al., 2007. Whole-body MR vascular screening detects unsuspected concomitant vascular disease in coronary heart disease patients. Eur. Radiol. 17, 1035–1045.
Ladd, S.C., Ladd, M.E., 2007. Perspectives for preventive screening with total body MRI. Eur. Radiol. 17, 2889–2897.
Lauenstein, T.C., Semelka, R.C., 2006. Emerging techniques: whole-body screening and staging with MRI. J. Magn. Reson. Imaging 24, 489–498.
Lesage, D., Angelini, E.D., Bloch, I., Funka-Lea, G., 2009. A review of 3D vessel lumen segmentation techniques: models, features and extraction schemes. Med. Image Anal. 13, 819–845.
Lind, L., Fors, N., Hall, J., Marttala, K., Stenborg, A., 2005. A comparison of three different methods to evaluate endothelium-dependent vasodilation in the elderly the prospective investigation of the vasculature in uppsala seniors (PIVUS) study. Arterioscler. Thromb. Vasc. Biol. 25, 2368–2375.
Lo, P., Van Ginneken, B., Reinhardt, J.M., Yavarna, T., De Jong, P.A., Irving, B., Fetita, C., Ortner, M., Pinho, R., Sijbers, J., et al., 2012. Extraction of airways from CT (EXACT'09). IEEE Trans. Med. Imaging 31, 2093–2107.
Lundberg, C., Johansson, L., Barbier, C.E., Lind, L., Ahlström, H., Hansen, T., 2013. Total atherosclerotic burden by whole body magnetic resonance angiography predicts major adverse cardiovascular events. Atherosclerosis 228, 148–152.
Madabhushi, A., Udupa, J.K., 2005. Interplay between intensity standardization and inhomogeneity correction in MR image processing. IEEE Trans. Med. Imaging 24, 561–576.
Matsuzaki, T., Oda, M., Kitasaka, T., Hayashi, Y., Misawa, K., Mori, K., 2015. Automated anatomical labeling of abdominal arteries and hepatic portal system extracted from abdominal CT volumes. Med. Image Anal. 20, 152–161.

Mori, K., Hasegawa, J., Suenaga, Y., Toriwaki, J., 2000. Automated anatomical labeling of the bronchial branch and its application to the virtual bronchoscopy system. IEEE Trans. Med. Imaging 19, 103–114.

Passat, N., Ronse, C., Baruthio, J., Armspach, J.-P., Maillot, C., 2006. Magnetic resonance angiography: from anatomical knowledge modeling to vessel segmentation. Med. Image Anal. 10, 259–274.

Pham, D.L., Prince, J.L., 1999. Adaptive fuzzy segmentation of magnetic resonance images. IEEE Trans. Med. Imaging 18, 737–752.

Pudney, C., 1998. Distance-ordered homotopic thinning: a skeletonization algorithm for 3D digital images. Comput. Vis. Image Understand. 72, 404–413.

van Rikxoort, E.M., Isgum, I., Arzhaeva, Y., Staring, M., Klein, S., Viergever, M.A., Pluim, J.P., van Ginneken, B., 2010. Adaptive local multi-atlas segmentation: application to the heart and the caudate nucleus. Med. Image Anal. 14, 39–49.

Rohlfing, T., Brandt, R., Menzel, R., Russakoff, D.B., Maurer Jr, C.R., 2005. Quo vadis, atlas-based segmentation? In: Handbook of Biomedical Image Analysis. Springer, pp. 435–486.

Rudyanto, R.D., Kerkstra, S., van Rikxoort, E.M., Fetita, C., Brillet, P.-Y., Lefevre, C., Xue, W., Zhu, X., Liang, J., Öksüz, İ., et al., 2014. Comparing algorithms for automated vessel segmentation in computed tomography scans of the lung: the VESSEL12 study. Med. Image Anal. 18, 1217–1232.

Ruehm, S.G., Goyen, M., Barkhausen, J., Kröger, K., Bosk, S., Ladd, M.E., Debatin, J.F., 2001. Rapid magnetic resonance angiography for detection of atherosclerosis. Lancet 357, 1086–1091.

Schaap, M., Metz, C.T., van Walsum, T., van der Giessen, A.G., Weustink, A.C., Mollet, N.R., Bauer, C., Bogunović, H., Castro, C., Deng, X., et al., 2009. Standardized evaluation methodology and reference database for evaluating coronary artery centerline extraction algorithms. Med. Image Anal. 13, 701–714.

Shahzad, R., Kirisli, H., Metz, C., Tang, H., Schaap, M., van Vliet, L., Niessen, W., van Walsum, T., 2013. Automatic segmentation, detection and quantification of coronary artery stenoses on CTA. Int. J. Cardiovasc. Imaging 29, 1847–1859.

Sled, J.G., Zijdenbos, A.P., Evans, A.C., 1998. A nonparametric method for automatic correction of intensity nonuniformity in MRI data. IEEE Trans. Med. Imaging 17, 87–97.

Suri, J., Wilson, D., Laxminarayan, S., 2007. Handbook of Biomedical Image Analysis: Volume 3: Registration Models. Springer Science & Business Media, Berlin, Heidelberg.

Suri, J.S., Liu, K., Reden, L., Laxminarayan, S., 2002a. A review on MR vascular image processing algorithms: acquisition and prefiltering: part I. IEEE Trans. Inf. Technol. Biomed. 6, 324–337.

Suri, J.S., Liu, K., Reden, L., Laxminarayan, S., 2002b. A review on MR vascular image processing: skeleton versus nonskeleton approaches: part II. IEEE Trans. Inf. Technol. Biomed. 6, 338–350.

Tizon, X., Lin, Q., Hansen, T., Borgefors, G., Johansson, L., Ahlström, H., Frimmel, H., 2007. Identification of the main arterial branches by whole-body contrast-enhanced MRA in elderly subjects using limited user interaction and fast marching. J. Magn. Reson. Imaging 25, 806–814.

Tschirren, J., McLennan, G., Palágyi, K., Hoffman, E.A., Sonka, M., 2005. Matching and anatomical labeling of human airway tree. IEEE Trans. Med. Imaging 24, 1540–1547.

Uchiyama, Y., Yamauchi, M., Ando, H., Yokoyama, R., Hara, T., Fujita, H., Iwama, T., Hoshi, H., 2006. Automated classification of cerebral arteries in MRA images and its application to maximum intensity projection. In: Proceedings of the 28th Annual International Conference of the IEEE EMBS (EMBS'06), pp. 4865–4868.

Van Leemput, K., Maes, F., Vandermeulen, D., Suetens, P., 1999. Automated model-based bias field correction of MR images of the brain. IEEE Trans. Med. Imaging 18, 885–896.

Wachinger, C., Glocker, B., Zeltner, J., Paragios, N., Komodakis, N., Hansen, M.S., Navab, N., 2008. Deformable mosaicing for whole-body MRI. In: Metaxas, D.N., Axel, L., Fichtinger, G., Székely, G. (Eds.), Medical Image Computing and Computer-Assisted Intervention. Springer, Berlin, Heidelberg, Germany, pp. 113–121.

Wells, W., Grimson, W., Kikinis, R., Jolesz, F., 1996. Adaptive segmentation of MRI data. IEEE Trans. Med. Imaging 15, 429–442.

Yang, G., Broersen, A., Petr, R., Kitslaar, P., de Graaf, M.A., Bax, J.J., Reiber, J., Dijkstra, J., 2011. Automatic coronary artery tree labeling in coronary computed tomographic angiography datasets. In: IEEE Comput. Cardiol., pp. 109–112.